American Mineralogist, Volume 99, pages 1528–1536, 2014

Spinels Renaissance: The past, present, and future of those ubiquitous minerals and materials

Bond-length fluctuation in the orthorhombic $3 \times 3 \times 1$ superstructure of $LiMn_2O_4$ spinel† 🔓

Nobuo Ishizawa[1,*], Kenji Tateishi[2], Shuji Oishi[3] and Shunji Kishimoto[4]

[1]Advanced Ceramics Research Center, Nagoya Institute of Technology, 10-6-29 Asahigaoka, Tajimi, 507-0071, Japan
[2]Gifu Prefectural Ceramics Research Institute, 3-11 Hoshigadai, Tajimi, Gifu 507-0811, Japan
[3]Faculty of Engineering, Shinshu University, 4-17-1 Wakasato, Nagano 380-8553, Japan
[4]Institute of Materials Structure Science, High Energy Accelerator Research Organization, 1-1 Oho, Tsukuba 305-0801, Japan

Abstract

Single-crystal synchrotron X-ray diffraction experiments are conducted on spinel-type $LiMn_2O_4$ at 230 and 320 K to investigate the effect of charge disproportionation of Mn ions on phase transition near room temperature. The orthorhombic $3a_c \times 3a_c \times 1a_c$ superstructure of the low-temperature form, where "a_c" is the ideal cubic cell edge, has a network of Mn^{4+} ions at the vertices of a slightly distorted truncated square tessellation comprising one square and two octagonal prisms; the square prism and one type of octagonal prism house Mn^{3+} ions with Jahn-Teller (JT) elongated Mn–O bonds almost parallel to the *c* and *b* axes, respectively, whereas the other octagonal prism houses Mn ions with JT-induced bond-length fluctuation for the Mn–O bonds lying almost parallel to the *a* axis. The Mn ions in the latter octagonal prism are assumed to exchange their oxidation states dynamically between 3+ and 4+ in a time ratio of ~3:1, forming a polaron centered at a Mn_4O_4 heterocubane cluster with orbital and spin orders. The high-temperature cubic form contains an inherent positional disordering of oxygen ions. The effect of the molecular polarons on the phase transition mechanism is discussed on the basis of a spin blockade in the form of truncated square tessellation.

Keywords: Lithium manganese oxide, $LiMn_2O_4$, low-temperature form, bond-length fluctuation, molecular polaron, spin blockade, phase transition, Mn_4O_4 heterocubane

Introduction

Lithium manganese oxide ($LiMn_2O_4$) undergoes a first-order structural phase transition near room temperature (Yamada and Tanaka 1995). The high-temperature form is an AB_2O_4 spinel-type with a normal cationic configuration, where A, B, and O are also designated as the tetrahedral and octahedral cation sites and oxygen ion site, having cubic $Fd\bar{3}m$ symmetry with a unit-cell dimension $a_c \approx 8.3$ Å. The low-temperature form crystallizes in orthorhombic *Fddd* symmetry, having unit-cell dimensions along **a** and **b** approximately triple that of the high-temperature prototype. This $3a_c \times 3a_c \times 1a_c$ (hereafter abbreviated as $3 \times 3 \times 1$) superstructure was first identified by a neutron powder diffraction and electron microscopy study (Rodríguez-Carvajal et al. 1998), and confirmed later by single-crystal synchrotron X-ray diffraction (Tateishi et al. 2004b).

This phase transition accompanies a charge disproportionation of Mn atoms occupying the octahedral B sites of the AB_2O_4 spinel. Since the mean oxidation state of Mn in $LiMn_2O_4$ is +3.5, the simplest scheme would be a disproportionation into Mn^{3+} and Mn^{4+} in equal fractions. However, the spinel-type structure, where the B-site ions are located at the nodes of a corner-linked tetrahedral network, does not allow alternative charge-ordering topologies, such as $–Mn^{3+}–Mn^{4+}–Mn^{3+}–Mn^{4+}–$, which have been more extensively studied for Fe^{2+} and Fe^{3+} ions at the B sites in magnetite with an inverse spinel-type structure, $^{iv}(Fe^{3+})^{vi}[Fe^{3+}_{1/2}Fe^{2+}_{1/2}]_2O_4$ (Verwey and de Boer 1936; Verwey and Haayman 1941; Sasaki 1997; Senn et al. 2012). The structural complexity of the low-temperature $LiMn_2O_4$ thus arises from frustrated charge disproportionation on the tetrahedral B-site network, which has not been fully solved to date.

This paper reports the novel occurrence of a bond-length fluctuation in selected Mn–O bonds within the $3 \times 3 \times 1$ superstructure of $LiMn_2O_4$, which can be interpreted as evidence of a dynamical charge exchange between 3+ and 4+ among the corresponding Mn ions. Although this phenomenon is considered an inherent characteristic of the low-temperature phase of $LiMn_2O_4$, the previous structure determination (Tateishi et al. 2004b) failed owing to a subtle alteration of the diffraction intensities, as expected from a complicated structure comprising 504 atoms at 18 crystallographically independent sites in a unit cell of ~5000 Å^3 in size. By utilizing a smaller crystal (~0.03 mm in size) with high-flux synchrotron X-rays to reduce the extinction problem, and a data collection strategy at significantly higher resolution ($d > 0.49$ Å) at a lower temperature (230 K) than used in the previous experiment (~0.05 mm, $d > 0.63$ Å, and 297 K), the present study is able to analyze unusual vibrational behavior at two oxygen ion sites via the split atom model.

Experimental detection of bond-length fluctuation in the Mn–O bonds indicates that an exchange in oxidation states of Mn between 3+ and 4+ occurs, because the Mn^{3+} in a high-spin

* E-mail: ishizawa@nitech.ac.jp

† 🔓 Open access: Article available to all readers online. Special collection papers can be found on GSW at http://ammin.geoscienceworld.org/site/misc/specialissuelist.xhtml.

0003-004X/14/0809–1528$05.00/DOI: http://dx.doi.org/10.2138/am.2014.4840

state electronic configuration ($t_{2g}^3e_g^1$) is stabilized in an elongated tetragonal dipyramid as a result of the Jahn-Teller (JT) distortion, in contrast with Mn^{4+} ($t_{2g}^3e_g^0$), which is stabilized in a relatively regular coordination octahedron (Moore and Janes 2004). The oxidation state can be estimated from the bond valence sum (BVS), which is a function of bond-length and number of bonds in the coordination sphere, using two empirical parameters (Brown 2002). If charge disproportionation occurs dynamically, then experimental detection of bond-length fluctuation and its separation into each component are thus essential in discussing the oxidation states of Mn, and, accordingly, the phase transition mechanism of the compound, which is mentioned in the Discussion section.

In addition, the Mn–O bond-length fluctuation appears to have a close relationship with the transport property of Li in the high-temperature form, which can be more broadly extended to "cubically stabilized $Li_x(Mn,M)_2O_{4-\delta}$ (M = Mg, Co, etc.)," a well-known candidate compound for a cathode material used in the Li ion battery (Park et al. 2010). The present study confirmed the structure model for the $1 \times 1 \times 1$ high-temperature form first proposed by Takahashi et al. (2003), in which the oxygen ions are distributed statically at the Wyckoff 96*g* site of the space group $Fd\bar{3}m$, in contrast with the widely used model that assumes the oxygen ions lie at the 32*e* site. In addition, it is pointed out that even the 96*g* model has a drawback in fully explaining the disordered distribution of Mn–O distances: an alternative model assuming the anharmonic vibration of oxygen ions, is also proposed.

Experimental procedures

Reagent-grade Li_2CO_3 and $MnCO_3$ were weighed and combined together to form a nominal 7 mol% $LiMn_2O_4$ mixture. Approximately 31.7 g of the mixture was placed in a platinum crucible and heated to 1373 K at a rate of 45 K/h in an air atmosphere. The peak temperature was maintained for 10 h, and then reduced to 723 K at 5 K/h with subsequent furnace-cooling by turning off the power. The flux was rinsed out with warm water. The crystals were black and octahedrally shaped, with a maximum size of approximately $0.1 \times 0.1 \times 0.1$ mm^3. The stoichiometric composition for the crystal is assumed as detailed in the Results section.

Preliminary single-crystal diffraction experiments were conducted using a three-circle imaging-plate diffractometer (Rigaku Rapid) with Mo*K*α X-rays. The phase transition temperature was determined by examining the appearance of superstructure reflections in oscillation photographs about the three principal axes of the high-temperature cubic form. During the cooling procedure, the [100] oscillation photograph at 295 K did not show any superstructure reflections, whereas they are clearly recorded in the next photograph taken at 293 K. The transition temperature of the sample during cooling was thus determined to be 294(1) K. Since it took approximately 10 min to decrease the temperature from 295 to 293 K, the mean cooling rate during transition was 0.2 K min^{-1}. The time required to take an oscillation photograph at a constant temperature was approximately 40 min. In a similar way, the transition temperature during heating was determined to be 310(1) K.

The synchrotron experiment was carried out at beamline 14A at the Photon Factory of the High Energy Accelerator Research Organization, Tsukuba, using a horizontal-type four-circle diffractometer (Satow and Iitaka 1989; Vaalsta and Hester 1997). The sample was first warmed, using a nitrogen gas stream, to 320 K, at which point the data collection was carried out over three days. The sample was then cooled at a rate of 2 K min^{-1} to 230 K, at which point another data collection was carried over four days. Cell dimensions were calculated at these temperatures from 24 reflections at $2\theta \approx 86°$. The cooling procedure from 320 to 230 K was interrupted several times to calculate cell dimensions at intermediate temperatures of 300, 280, and 250 K, using 12 reflections at $2\theta \approx 56°$ and $2\theta \approx 66°$.

Intensity data were collected for the hemisphere of reciprocal space in the range $1° < 2\theta < 100°$ at 230 K, and the full sphere in the range $1° < 2\theta < 130°$ at 320 K. An *F* lattice centering was assumed for both data collections according to the previous study (Tateishi et al. 2004b). An eight-channel avalanche photodiode detector (Kishimoto et al. 1998), possessing a large dynamic range (up to ~5×10^8 cps) for the X-rays employed allowed for the elimination of all the attenuators and absorbers along the X-ray path. The wavelength of the X-rays emitted from the vertical wiggler was calibrated using a silicon single crystal to be 0.75064 Å at 230 K and 0.75059 Å at the other temperatures, including 320 K.

The crystallography program packages Xtal (Hall et al. 2002) and Jana2006 (Petricek et al. 2006) were used for data processing and structure refinement, respectively. An extinction correction was applied according to Becker and Coppens formalism (Becker and Coppens 1974). The anomalous scattering factors and the X-ray absorption coefficients at the experimental wavelength were taken from the Sasaki tables (Sasaki 1989, 1990). The values of the BVSs were calculated according to Brown and Altermatt (1985) with their parameter values. The computer programs Diamond (Brandenburg and Putz 2005) and Vesta (Momma and Izumi 2011) were used for visualization of crystal structures and volumetric data.

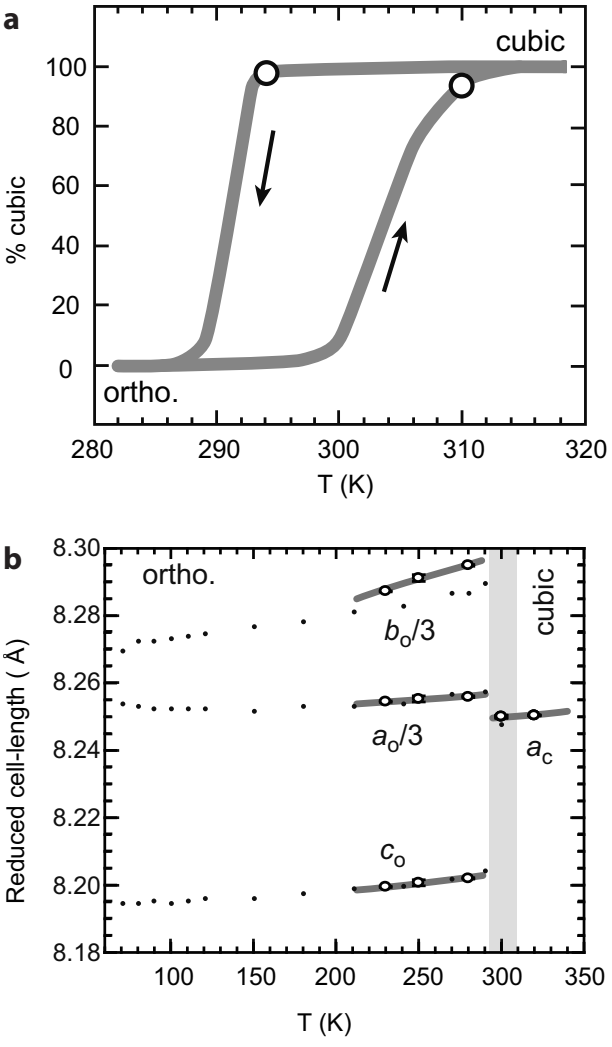

Figure 1. Phase transition temperatures and changes in cell dimensions with temperature: (**a**) phase transition temperatures (open circles) of the present crystal superimposed on changes of the volume fraction of the high-temperature cubic phase with temperature (gray curve), given in Figure 4 of the paper by Rousse et al. (1999b), and (**b**) changes in cell dimensions during cooling (open circles on gray curves) obtained in the present study, in comparison with dotted data given in Figure 9 of the paper by Rousse et al. (1999b) during heating. The estimated uncertainties are approximately equal to the size of circles.

Results

Phase-transition temperatures and cell dimensions

The transition temperatures of 294(1) and 310(1) K, determined from the appearance and disappearance of superstructure reflections during cooling and heating, respectively, are plotted in Figure 1a. These values were very close to the onset and endpoint of the changes in volume fraction of the high- and low-temperature forms observed by the neutron powder diffraction (Rousse et al. 1999b). Cell dimensions (a_o, b_o, and c_o for the orthorhombic low-form, and a_c for the cubic high-form) at various temperatures during cooling are given in Table 1, and plotted in Figure 1b, together with data reported by Rousse et al. (1999b). A small difference in $b_o/3$ just below the transition point could be ascribed to the experimental method; the single-crystal sample of $0.03 \times 0.03 \times 0.03$ mm^3 used in the present study remained a mono-domain (no twinning) during cooling across the transition, and the profile decomposition analysis employed in the powder diffraction method was not required in the present study.

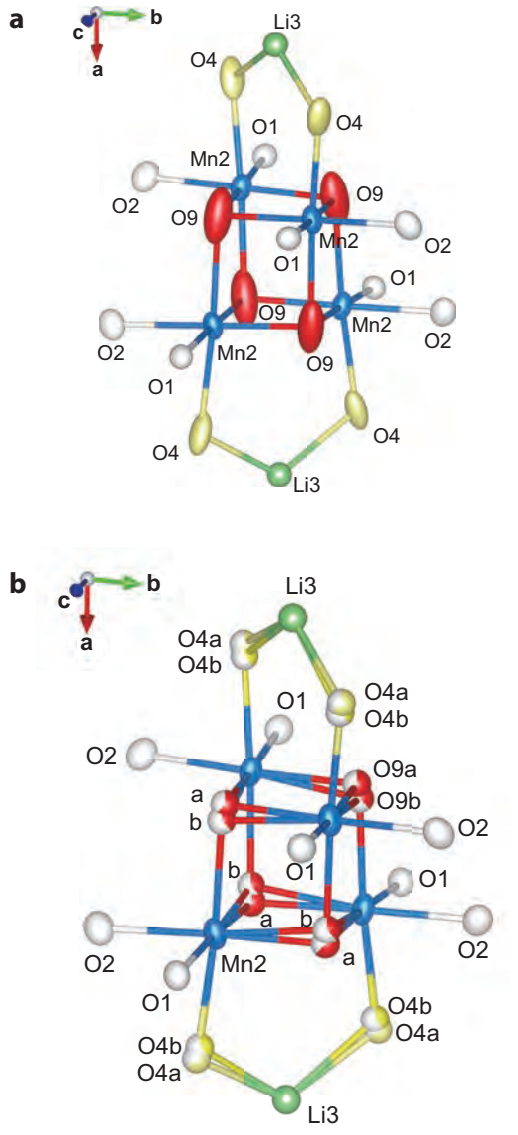

Figure 2. The local structures around the $Mn2_4O9_4$ heterocubane in $LiMn_2O_4$ at 230 K: (**a**) the non-split atom model with anisotropic ADP for O and Mn and isotropic ADP for Li at 230 K; and (**b**) the split atom model for O4 and O9 with isotropic ADP. Some atom labels of $Mn2_4O9_4$ heterocubane in **b** are abbreviated, as "a" for O9a and "b" for O9b for clarity. The occupation at the split atom sites is shown by the pie charts on the atoms in **b**.

Low-temperature form at 230 K

Crystal data for $LiMn_2O_4$ at 230 K and a summary of the refinements are given in Table 2. Final atomic positions and atomic displacement parameters are given in Table 3. The origin of the space group *Fddd* was chosen at an inversion center (origin choice 2). The structural refinement, assuming an ordered (non-split) atom model (Tateishi et al. 2004b), converged with R/wR = 0.0284/0.0433, using 134 refinable parameters for 3313 reflections, which have an observed diffraction intensity larger than three times the estimated standard uncertainty [$I > 3\sigma(I)$]. The occupation parameters of the nine O sites were also examined simultaneously, but no significant deviation from unity was detected; they were 0.989(8), 0.977(8), 0.986(8),

Table 1. Cell dimensions of $LiMn_2O_4$ during cooling

Temperature (K)	a (Å)	b (Å)	c (Å)	Space group
320	8.2513(1)			$Fd\bar{3}m$
300	8.2500(4)			$Fd\bar{3}m$
280	24.768(1)	24.885(1)	8.2020(2)	*Fddd*
250	24.766(3)	24.874(3)	8.2007(9)	*Fddd*
230	24.764(2)	24.862(2)	8.1995(8)	*Fddd*

Table 2. Crystal data and summary of the refinements for the $3\times3\times1$ superstructure of $LiMn_2O_4$ at 230 K in comparison with the 96*g* model of the $1\times1\times1$ spinel-type high-temperature form at 320 K

Form	Low-temperature form	High-temperature form
Model name	O9O4split	96*g*
Temperature (K)	230	320
a (Å)	24.764(2)	8.2513(1)
b (Å)	24.862(2)	8.2513(1)
c (Å)	8.1995(8)	8.2513(1)
V (Å^3)	5048.1(8)	561.78(1)
Space group	*Fddd*	$Fd\bar{3}m$
N_{meas}	13845	8316
θ_{max} (°)	49.97	64.84
R_{int}	0.018	0.025
N_{ref}	3313	236
N_{ref} [$I > 3\sigma(I)$]	3313	208
R [$I > 3\sigma(I)$]	0.0279	0.0117
wR [$I > 3\sigma(I)$]	0.0430	0.0159
Weighting scheme	$w = 1/[\sigma^2(F)+0.0001\,F^2]$	$w = 1/[\sigma^2(F)+0.0001\,F^2]$
S	1.87	1.39
N_{params}	132	11
ρ_{max}	0.75	0.92
ρ_{min}	−0.79	−0.40
Extinction	790(40)	450(60)
Atomic parameters	See Table 3	Li at (1/8, 1/8, 1/8), U_{eq} = 0.0124(3) Mn at (1/2,1/2,1/2), U_{eq} = 0.01020(2) O at (x, x, z); x = 0.26898(15), z = 0.2506(3), U_{eq} = 0.0134(3), Occ = 1/3

Notes: N_{meas}, N_{ref}, and N_{params} are the numbers of reflections measured, crystallographically independent reflections used for refinements, and structural parameters refined, respectively. U_{eq} is the equivalent isotropic ADP calculated from the anisotropic U^{ij}. See details in the supplementary CIF file[1].

TABLE 3. Atomic positions and displacement parameters of the $3 \times 3 \times 1$ superstructure of $LiMn_2O_4$ at 230 K

Atom	Site occupancy	*x*	*y*	*z*	U_{iso}/U_{eq}	U^{11}	U^{22}	U^{33}	U^{12}	U^{13}	U^{23}
Mn1	1	0.25	0.25	0.5	0.00492(8)	0.00473(13)	0.00448(12)	0.00553(15)	–0.00027(11)	–0.00111(11)	–0.00038(11)
Mn2	1	0.080799(13)	0.085516(11)	0.50091(4)	0.00453(5)	0.00647(10)	0.00338(9)	0.00374(10)	–0.00068(8)	–0.00047(7)	–0.00019(7)
Mn3	1	0.084147(13)	0.330131(12)	0.24966(4)	0.00435(5)	0.00428(9)	0.00483(9)	0.00394(9)	0.00071(7)	0.00030(7)	–0.00057(7)
Mn4	1	0.253405(12)	0.167979(11)	0.24512(4)	0.00387(5)	0.00407(9)	0.00378(8)	0.00377(10)	0.00042(7)	0.00046(7)	–0.00054(8)
Mn5	1	0.166740(11)	0.243849(12)	0.24376(4)	0.00395(5)	0.00361(9)	0.00406(9)	0.00419(10)	0.00027(7)	–0.00036(8)	0.00013(7)
Li1	1	0.125	0.125	0.125	0.0107(15)						
Li2	1	0.375	0.21309(18)	0.375	0.0012(7)						
Li3	1	0.2052(2)	0.375	0.375	0.0050(9)						
Li4	1	0.29002(18)	0.2943(2)	0.1227(5)	0.0102(7)						
O1	1	0.17436(6)	0.16781(5)	0.26212(18)	0.0051(2)	0.0056(5)	0.0047(4)	0.0050(4)	–0.0001(4)	–0.0003(4)	0.0007(4)
O2	1	0.07878(6)	0.00765(6)	0.47870(19)	0.0061(3)	0.0069(5)	0.0059(4)	0.0054(5)	–0.0008(4)	0.0010(4)	–0.0004(4)
O3	1	0.07897(6)	0.33141(6)	0.48165(19)	0.0057(3)	0.0057(5)	0.0061(4)	0.0054(4)	–0.0007(4)	–0.0011(4)	–0.0018(4)
O4a	0.62(5)	0.2558(4)	0.17353(15)	0.4741(5)	0.0048(3)						
O4b	0.38(5)	0.2482(6)	0.1720(2)	0.4812(9)	0.0048(3)						
O5	1	0.00657(6)	0.00694(5)	0.23681(19)	0.0051(3)	0.0051(4)	0.0040(4)	0.0061(5)	0.0003(3)	–0.0001(4)	0.0001(4)
O6	1	0.25635(6)	0.09033(5)	0.23907(18)	0.0046(3)	0.0050(5)	0.0048(4)	0.0040(4)	–0.0010(3)	–0.0005(4)	0.0004(4)
O7	1	0.16285(6)	0.32245(5)	0.23581(17)	0.0050(3)	0.0059(5)	0.0042(4)	0.0048(4)	0.0007(3)	–0.0004(4)	0.0001(3)
O8	1	0.09053(5)	0.24332(6)	0.23415(19)	0.0053(3)	0.0034(4)	0.0068(4)	0.0058(5)	–0.0012(3)	0.0009(4)	0.0011(4)
O9a	0.62(2)	0.0797(2)	0.16069(11)	0.5194(4)	0.0063(3)						
O9b	0.38(2)	0.0905(4)	0.16210(19)	0.5123(7)	0.0063(3)						

Notes: U_{eq} is the equivalent isotropic ADP calculated from the anisotropic U^{ij}.

TABLE 4. Eigenvalues of the ADP ellipsoids, U^1, U^2, and U^3 (Å^2) in ascending order[a]

	230 K				297 K			
	U^1	U^2	U^3	U^3/U^1	U^1	U^2	U^3	U^3/U^1
Mn1	0.0037	0.0047	0.0063	1.67	0.0072	0.0104	0.0111	1.53
Mn2	0.0031	0.0038	0.0067	2.16	0.0076	0.0102	0.0120	1.58
Mn3	0.0033	0.0045	0.0053	1.62	0.0068	0.0085	0.0133	1.95
Mn4	0.0028	0.0043	0.0044	1.55	0.0070	0.0086	0.0111	1.58
Mn5	0.0033	0.0042	0.0043	1.28	0.0064	0.0085	0.0111	1.74
O1	0.0043	0.0048	0.0057	1.35	0.0067	0.0099	0.0120	1.80
O2	0.0043	0.0055	0.0084	1.95	0.0080	0.0104	0.0129	1.61
O3	0.0032	0.0065	0.0081	2.53	0.0067	0.0108	0.0153	2.28
O4	0.0036	0.0059	0.0158	4.4*	0.0098	0.0118	0.0173	1.78
O5	0.0040	0.0050	0.0056	1.4	0.0077	0.0102	0.0126	1.63
O6	0.0040	0.0043	0.0065	1.62	0.0078	0.0102	0.0108	1.38
O7	0.0040	0.0045	0.0060	1.5	0.0074	0.0099	0.0132	1.78
O8	0.0029	0.0054	0.0076	2.65	0.0054	0.0093	0.0156	2.89
O9	0.0056	0.0068	0.0270	4.8*	0.0100	0.0112	0.0305	3.05
Average	0.0047	0.0050	0.0075	1.58	0.0093	0.0101	0.0123	1.32

[a] Data are obtained from the non-split atom model refinements at 230 K [R = 2.84% for 3313 reflections with $I > 3\sigma(I)$] and 297 K [R = 3.83% for 1547 reflections with $I > 3\sigma(I)$ after Tateishi et al. 2004b]. The unusually large values for O9 and O4 are marked with asterisks (see text).

1.001(8), 0.981(8), 0.988(8), 1.003(8), 0.996(8), and 1.001(9) for O1 through O9, respectively. However, the anisotropic atomic displacement parameter (ADP) ellipsoids of O9 and O4 were extraordinarily elongated toward **a**, as shown in Figure 2a. The ratios of the maximum and minimum eigenvalues (U^3/U^1) of the O9 and O4 ellipsoids are 4.8 and 4.4, respectively, which is in contrast to the other more moderate values, which ranged between 1.35 and 2.65; these are given in Table 4. A comparison between the ADP ellipsoids shows that the maximum eigenvalues U^3 for O9 and O4 remain almost unchanged by cooling the crystal from 297 to 230 K, whereas all the other eigenvalues are reduced by approximately half. The difference Fourier synthesis eliminating O9 or O4 for phasing resulted in an asymmetric electron density distribution along a direction almost parallel to the *a* axis, suggesting a possible positional disorder owing to the bond-length fluctuation of Mn2–O9 and Mn2–O4.

Assuming the split atom model as shown in Figure 2b, and employing O9a/O9b instead of O9, and O4a/O4b instead of O4, further refinements converged with lower *R*/*wR* values (0.0279/0.0430) using a lower number of refinable parameters (132). In the course of refinement, the same isotropic ADP was assumed for the O9a–O9b split pair, as well as for the O4a–O4b pair, and the sums of the split site populations were assumed to be unity for both pairs. The populations of O9a and O4a converged to almost the same value, i.e., 0.62(2) for O9a and 0.62(5) for O4a, suggesting a high structural correlation between the O9 and O4 splits, as discussed later. Hereafter, the Mn coordination sphere including O4a and/or O9a is denoted as "a-type" and the sphere including O9b and/or O4b is denoted as "b-type". The Mn–O bond lengths and the BVSs are summarized in Table 5. As discussed later, the lengths are listed only for the a-type and b-type, and not for the combination. The distribution of Mn–O bond lengths is illustrated in Figure 3. The crystallographic information file (CIF) of the 230 K data set is available as a deposit[1].

High-temperature form at 320 K

Assuming the ideal spinel-type atomic arrangement for the stoichiometric $LiMn_2O_4$, i.e., Li at 8*a* (1/8, 1/8, 1/8), Mn at 16*d* (1/2, 1/2, 1/2), and O at 32*e* (*x*, *x*, *x*), where $x = 0.2634$ in $Fd\bar{3}m$, the harmonic refinement converged with $R/wR = 0.0245/0.0401$ for 208 reflections with $I > 3\sigma(I)$ using eight parameters. If the nonstoichiometry of oxygen ions was taken into consideration, then the refinement converged with $R/wR = 0.0254/0.0399$ for 208 reflections with $I > 3\sigma(I)$ using nine parameters. The occu-

[1] Deposit item AM-14-804, CIF. Deposit items are stored on the MSA web site and available via the *American Mineralogist* Table of Contents. Find the article in the table of contents at GSW (ammin.geoscienceworld.org) or MSA (www.minsocam.org), and then click on the deposit link.

TABLE 5. The Mn–O and Li–O bond lengths (Å) in $LiMn_2O_4$ at 230 K

Atom pairs	O4a and O9a	O4b and O9b
Mn1–O2[i]	1.9679(15)	
Mn1–O2[ii]	1.9679(15)	
Mn1–O4	1.918(4)	1.945(6)
Mn1–O4[iii]	1.918(4)	1.945(6)
Mn1–O5[i]	2.1711(16)*	
Mn1–O5[ii]	2.1711(16)*	
Mean	2.019	2.028
BVS	3.10(1)	3.01(1)
Oxidation state	3+	3+
Mn2–O1[i]	1.9638(15)	
Mn2–O2	1.9451(15)	
Mn2–O4[i]	2.167(9)*	1.972(15)
Mn2–O9	1.875(3)	1.921(5)
Mn2–O9[i]	2.223(3)*	1.952(4)
Mn2–O9[iv]	1.886(3)	1.958(5)
mean	2.010	1.952
BVS	3.25(1)	3.58(3)
Oxidation state	3+	4+
Mn3–O3	1.9068(16)	
Mn3–O3[v]	2.2083(14)*	
Mn3–O6[vi]	1.9454(15)	
Mn3–O7	1.9617(15)	
Mn3–O7[vii]	1.9416(15)	
Mn3–O8	2.1679(15)*	
Mean	2.022	
BVS	3.10(1)	
Oxidation state	3+	
Mn4–O1	1.9624(15)	
Mn4–O3[viii]	1.8745(16)	
Mn4–O4	1.883(4)	1.942(7)
Mn4–O5[i]	1.8841(14)	
Mn4–O6	1.9324(14)	
Mn4–O6[ix]	1.9328(16)	
Mean	1.912	1.921
BVS	4.00(1)	3.89(1)
Oxidation state	4+	4+
Mn5–O1	1.9058(14)	
Mn5–O2[i]	1.9300(16)	
Mn5–O5[i]	1.9000(14)	
Mn5–O7	1.9576(14)	
Mn5–O8	1.8888(14)	
Mn5–O8[vii]	1.8775(16)	
Mean	1.910	
BVS	4.01(1)	
Oxidation state	4+	

TABLE 5.—*CONTINUED*

Atom pairs	O4a and O9a	O4b and O9b
Li1–O1	1.9726(14)	
Li1–O1[i]	1.9726(14)	
Li1–O1[vii]	1.9726(14)	
Li1–O1[ix]	1.9726(14)	
Mean	1.973	1.973
BVS	1.02(1)	1.02(1)
Li2–O2[ii]	1.994(3)	
Li2–O2[x]	1.994(3)	
Li2–O3[iii]	1.976(3)	
Li2–O3[viii]	1.976(3)	
Mean	1.985	1.985
BVS	0.98(1)	0.98(1)
Li3–O4[iii]	1.980(6)	2.022(11)
Li3–O4[x]	1.980(6)	2.022(11)
Li3–O7	2.027(3)	
Li3–O7[v]	2.027(3)	
Mean	2.004	2.025
BVS	0.94(1)	0.88(1)
Li4–O5[i]	1.957(5)	
Li4–O6[x]	1.957(5)	
Li4–O8[viii]	1.932(5)	
Li4–O9[viii]	1.914(5)	2.011(6)
Mean	1.940	1.964
BVS	1.11(1)	1.04(1)

Notes: Distances related to the split atom sites (a, b) for O4 and O9 are given in separate columns where duplication is suppressed. The Mn–O bonds elongated by the Jahn-Teller effect are marked with asterisks. The mean Mn–O bond lengths, bond valence sums (BVS), and presumed oxidation states for Mn are also given. Symmetry operations: (i) –x+5/4,–y+5/4,z; (ii) x+1/4,y+1/4,–z+1; (iii) –x+1/2,–y+1/2, –z+1; (iv) x,–y+5/4,–z+9/4; (v) x,–y+3/4,–z+3/4; (vi) x–1/4,y+1/4,–z+1/2; (vii) –x+5/4,y, –z+5/4; (viii) x+1/4,–y+1/2,z–1/4; (ix) x,–y+5/4,–z+5/4; (x) –x+1/2,y+1/4,z–1/4.

pation parameter of the oxygen ion site converged at 0.970(19), which corresponds to $\delta = 0.12(8)$ in the expression $LiMn_2O_{4-\delta}$. Relatively large positive and negative residual electrons of ±1.2 *e* Å^{-3} were found at positions 0.3–0.4 Å apart from the O site, which could be ascribed to either positional disorder or the anharmonic vibrational nature of the oxygen ion. Further refinement was carried out, assuming the oxygen ion with harmonic vibration lay at the Wyckoff 96*g* site with 1/3 site occupancy, and converged with $R/wR = 0.0117/0.0159$ using 11 parameters. Other models assuming anharmonic vibration of the oxygen ion at the 32*e* site were also examined. Refinements using the third-order Gram-Charlier series expansion for the oxygen ion converged with $R/wR = 0.0134/0.0188$ using 11 parameters, and those using up to the fourth-order terms converged with $R/wR = 0.0117/0.0157$ using 15 parameters. The *R* factors of the harmonic 96*g* and the anharmonic 32*e* models were significantly lower than those of the harmonic 32*e* model. In addition, there were negligibly few residual electrons near the O sites in the former two models and distribution of electrons did not form any peculiar shape. These results suggested that the harmonic 96*g* and/or the anharmonic 32*e* models are more appropriate for describing the high-temperature form than the conventional harmonic 32*e* model.

The δ value in $LiMn_2O_{4-\delta}$ estimated from the population refinement of the oxygen deficiency became –0.06(4) for both the harmonic 96*g* and anharmonic 32*e* models, in contrast with 0.12(8) for the harmonic 32*e* model. It should be noted that the δ value in the former two models was much closer to null than that in the latter, as discussed later. The stoichiometric composition (i.e., $\delta = 0$) was thus assumed for the present crystal.

The 96*g* model gives 1.974(2) Å for the Li–O bond length, and two different bond lengths of 2.070(3) and 1.913(1) Å for Mn–O, in agreement with Takahashi et al. (2003). The frequency ratio of the longer and shorter Mn–O bonds is 1:2, which is imposed by the symmetry of the structure model. The longer and shorter Mn–O bond lengths at 320 K are also compared to the distribution of Mn–O bond lengths in the low-temperature form at 230 K in Figure 3.

Crystal data and selected structural parameters of the harmonic 96*g* model of the high-temperature form are given in Table 2. Full information about the harmonic 96*g* and the anharmonic 32*e* models using the third- and fourth-order expansions, respectively, are given consecutively as a deposit[1].

DISCUSSION

Oxidation state of manganese

The oxidation states of Mn1 and Mn3 are essentially +3 as seen from the BVSs in Table 5. This agrees well with what would be expected from the existence of typical pseudo-tetragonal JT

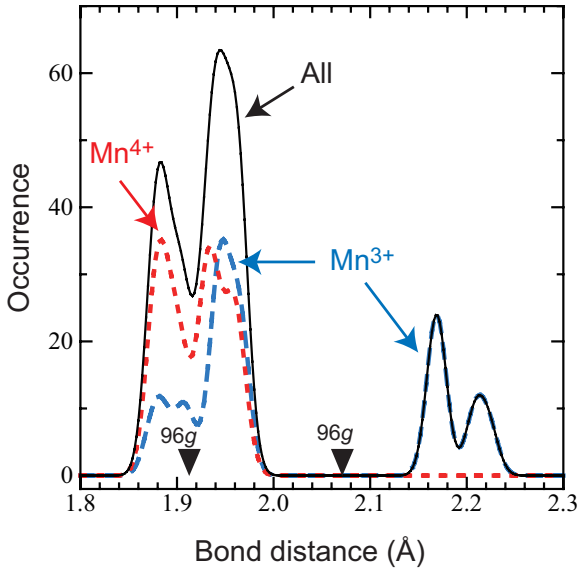

FIGURE 3. Distribution of Mn–O bond lengths in the low-temperature form at 230 K. The solid line shows the occurrence of six bonds of a manganese ion, with each bond profile assuming a normal distribution function with a full-width at half maximum of 0.02 Å. The vertical axis is scaled so that the integration over all the Mn–O bond distances becomes six. The long- and short-dashed lines shows the contributions of Mn^{3+}–O and Mn^{4+}–O bonds to the solid line, respectively. The two filled triangles labeled 96*g* are the longer and shorter Mn–O bond lengths obtained from the harmonic 96*g* model for the high-temperature form at 320 K.

distortion in an octahedral coordination geometry; two long bonds of ~2.2 Å (Mn1–$O5^{i}$ and Mn1–$O5^{ii}$ for $Mn1O_6$; Mn3–$O3^{v}$ and Mn3–O8 for $Mn3O_6$) compared with the mean of ~2.02 Å. The JT-elongated bonds lie almost parallel to **c** for Mn1 and to **b** for Mn3. On the other hand, Mn4 and Mn5 are essentially +4, as seen from the BVSs in Table 5. This is also consistent with the shape of the coordination octahedra, having almost equidistant Mn–O bonds with a mean of ~1.91 Å (Table 5 and Fig. 3). The split atom sites, O4a and O4b, are also involved in the Mn4–O bonds, which vary between 1.883(4) and 1.942(7) Å, depending on the split atom positions, though they do not elongate to a large degree like the Mn^{3+} JT bond of ~2.2 Å because the split occurs almost tangentially to the Mn4 coordination sphere. The difference in the mean Mn4–O bond distance between the a- and b-type Mn4 octahedra is as marginal as ~0.01 Å, suggesting an invariable nature of the oxidation state for Mn4 against the O site splits. All these data support the fact that Mn cations at the Mn1 and Mn3 sites are primarily 3+, and those at Mn4 and Mn5 sites are primarily 4+, which is in agreement with the results by Rodríguez-Carvajal et al. (1998) and Tateishi et al. (2004b).

Contrary to the tangential case for Mn4, the oxidation state of Mn2 is significantly affected by the O site splits because the split occurs nearly radially for the Mn2 coordination. If the oxygen ions occupy the O9a and O4a sites to form the a-type Mn2 octahedron, then the shape of the $Mn2O_6$ octahedron is deformed like $Mn1^{3+}$- or $Mn3^{3+}$-bearing octahedra, except that the two JT-elongated Mn2–O9a and Mn2–O4a bonds of ~2.2 Å lie almost parallel to **a** (Fig. 2b and Table 5). The BVS of +3.25 also favors the oxidation state of 3+ for Mn2. On the other hand, if the oxygen ions occupy the O9b and O4b sites to form the b-type Mn2 octahedron, four of the six Mn2–O bonds are altered so that they become very similar in length to each other, having a mean of ~1.95 Å (Table 5). Therefore, the oxidation state of Mn2 in the b-type Mn2 octahedron is assumed to be 4+.

The calculated BVS of +3.58 for the b-type Mn2 octahedron is slightly lower than the assumed value (4+). This could be ascribed to the geometrical constraint in the second coordination sphere of Mn2, as shown in Figure 2b. The O4 atom pairs surrounding the $Mn2_4O9_4$ heterocubane are capped by Li3 at the top and bottom ends along **a**. A shortening of Mn2-O4b, therefore, induces an elongation of Li3–O4b to 2.02 Å, resulting in the longest mean Li–O (2.03 Å) and the smallest BVS (+0.88) for Li3. This length is considerably longer and the BVS is considerably smaller than those of the other Li ions (1.94–1.99 Å and +0.98–1.11), as given in Table 5. This could be the reasons why $Mn2^{4+}$–O4b (1.97 Å) cannot contract to the same level as $Mn2^{4+}$–O9b (1.95 Å), and, accordingly, the calculated BVS for $Mn2^{4+}$ (+3.58) does not reach the expected value of +4.

The ideal disproportionation scheme for Mn2 can be summarized as follows: when its octahedron is of the a-type, the oxidation state of Mn2 is 3+, and when its octahedron is of the b-type, the oxidation state of Mn2 is 4+. This scheme explains the virtually identical population ratios of O9a/O9b and O4a/O4b obtained by the structural refinements, because the two oxygen ions are displaced from O4b and O9b to O4a and O9a, respectively, by the JT elongation at the same time that the oxidation state of the central Mn2 turns into 3+, and the reverse takes place when Mn2 turns into 4+. The refined populations of the O9 and O4 split pairs thus directly indicate the probabilities of the two oxidation states of Mn2, i.e., a 3+ oxidation state for Mn2 is 62% and that of 4+ is 38%, leading to an oxidation state for Mn2 of +3.38, as an average over time and space.

This ideal charge disproportionation scheme can be examined in light of the charge neutrality principle of the crystal. The number of Mn sites in the $3 \times 3 \times 1$ superstructure containing 72 $LiMn_2O_4$ chemical units in a unit cell is 16 for Mn1 and 32 for each of Mn2, Mn3, Mn4, and Mn5. The assumed oxidation states of 3+ for all Mn1 and Mn3 sites, and 4+ for all Mn4 and Mn5 sites result in the oxidation state of +3.25 for Mn2. This value corresponds to a state in which the $Mn2_4O9_4$ heterocubane structure consists of three $Mn2^{3+}$ and one $Mn2^{4+}$, i.e., a 3:1 ratio. The percentage of $Mn2^{3+}$ (75%) is slightly larger than the experimentally obtained value of 62%, although the estimated standard uncertainty of 2–5% may partially account for the difference.

Molecular polaron with bond-length fluctuation

The split of the O9 and O4 atom sites owing to JT distortion along **a**, and the disproportionation scheme for Mn2 into 75% Mn^{3+} and 25% Mn^{4+} could be modeled into the formation of a molecular polaron with bond-length fluctuation, as illustrated in Figure 4. The four Mn2 ions in the $Mn2_4O9_4$ heterocubane structure with a ground state of $t_{2g}^3 e_g^1$ (Mn^{3+} with a high-spin electronic configuration) have an orbital order such that the half-occupied $d(3x^2 - r^2)$ orbital is directed nearly parallel to **a**, with one hole shared among them, enabling bond-length fluctuation along it.

To continue hole hopping over just the four Mn ions of the

$Mn2_4O9_4$ heterocubane, the following two conditions must be satisfied: (1) the $d(3x^2 - r^2)$ orbital of the four Mn2 ions in the heterocubane are ordered in the spin state, and (2) the $Mn2_4O9_4$ heterocubane is isolated from its surroundings by the spin blockade (Maignan et al. 2004; Weinmann et al. 1995), which limits the hole hopping strictly to within the heterocubane structure.

As shown in Figure 5, Mn_4O_4 heterocubanes form a corner-shared network in the spinel structure. In the $3 \times 3 \times 1$ superstructure of $LiMn_2O_4$, there are four types of heterocubanes: $Mn2_4O9_4$, $Mn3_2Mn4_2O3_2O6_2$, $Mn3_2Mn5_2O7_2O8_2$, and Mn1Mn2Mn4Mn5O1O2O4O5. The $Mn2_4O9_4$ heterocubane is corner-linked to the four Mn1Mn2Mn4Mn5O1O2O4O5 heterocubanes via Mn2. Therefore, $Mn1^{3+}$, $Mn4^{4+}$, and $Mn5^{4+}$ should be in the opposite spin state to Mn2 to establish the spin blockade for at least the nearest Mn–Mn neighbors. Since $Mn3^{3+}$ is not included in any of the four heterocubanes corner-linked to $Mn2_4O9_4$, it still retains freedom in its spin state. A precise and accurate neutron diffraction study would be necessary for further discussion of the spin states of Mn in the $3 \times 3 \times 1$ superstructure.

The Mn–O bond-length fluctuation is expected to occur in Mn-bearing perovskite-type oxides by the superexchange interaction (Goodenough et al. 2003), where oxygen forms an ~180° bridge between two adjacent Mn ions. To the best of the authors' knowledge, this study has shown the first experimental evidence of the occurrence of bond-length fluctuations in Mn-bearing spinel-type oxides with an ~90° bridge, although Yamada et al. (1979) first suspected that the Fe_4O_4 heterocubane in magnetite behaves as a molecular polaron.

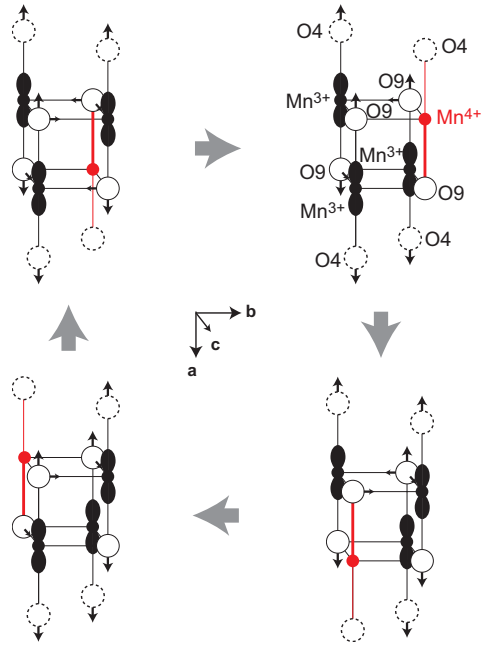

FIGURE 4. Schematic diagram of the bond-length fluctuation in the molecular polaron centered at the $Mn2_4O9_4$ heterocubane. The half-filled $d(3x^2 - r^2)$ orbital is illustrated in black for three $Mn2^{3+}$, and the empty one by a small filled circle in red for $Mn2^{4+}$. The O9 and O4 atoms are indicated by solid and dashed open circles, respectively, with the Jahn-Teller distortions shown by small black arrows. An example sequence of fluctuations is shown by gray arrows.

Origin of the orthorhombicity

The Mn^{4+} ions at the Mn4 and Mn5 sites projected along **c** exist at the vertices of a tessellation consisting of two octagons and one square, slightly distorted, as shown in Figure 6. This is essentially a "truncated square tessellation," among the eight semi-regular ones (Grunbaum and Shephard 1987). The square prism of the tessellation houses an array of $Mn1^{3+}$ parallel to **c** with JT elongation almost parallel to **c**. The one octagonal prism houses $Mn3^{3+}$ about the twofold screw axis parallel to **c**, whereas the other octagonal prism houses the $Mn2_4O_4$ heterocubane centered at the Wyckoff 8*b* sites of *Fddd*, having point symmetry of 222. The former $Mn3^{3+}$-bearing octagonal prism is elongated along **b** owing to the JT distortion almost parallel to this direction, whereas the latter Mn2-bearing octagonal prism is elongated along **a** to a lesser extent, owing to JT-induced bond-length fluctuation almost parallel to this direction. If all the Mn2 is 3+ similar to $Mn3^{3+}$, then the degrees of JT distortions along **a** and **b** should become the same. The $3 \times 3 \times 1$ superstructure would then exhibit the truncated square tessellation in its ideally tetragonal form, which contradicts the metrically orthorhombic nature of the low-temperature form. Conversely, the orthorhombicity of the $3 \times 3 \times 1$ superstructure can be ascribed to the attenuated JT-elongation along **a** compared with **b**, owing to a dynamic exchange of the oxidation state of Mn2 between 3+ and 4+, associated with the bond-length fluctuation.

Role of polarons in the orthorhombic–cubic phase transition of $LiMn_2O_4$

In the $3 \times 3 \times 1$ superstructure of $LiMn_2O_4$, the molecular polaron is centered only at the $Mn2_4O9_4$ heterocubane. The

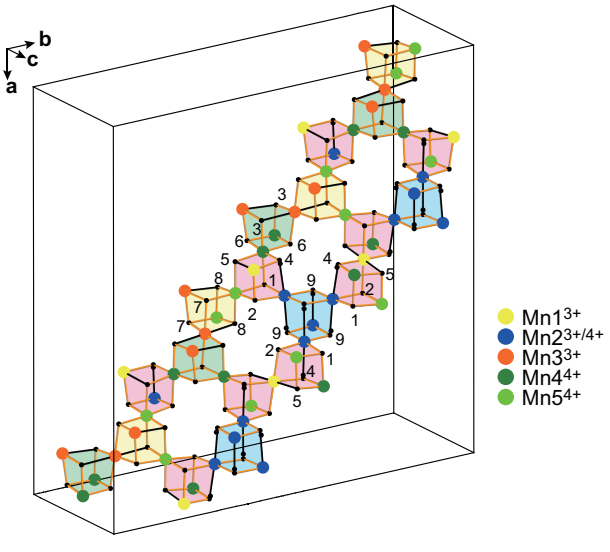

FIGURE 5. The corner-sharing connections of the Mn_4O_4 heterocubanes in a structural moiety cutting out parallel to (110) of the low-temperature form of the $LiMn_2O_4$ spinel. The lithium atoms are eliminated for clarity. The four types of Mn_4O_4 heterocubanes, i.e., $Mn2_4O9_4$, $Mn3_2Mn4_2O3_2O6_2$, $Mn3_2Mn5_2O7_2O8_2$, and Mn1Mn2Mn4Mn5O1O2O4O5 are shaded with different colors. The Jahn-Teller elongated Mn^{3+}–O bonds are colored in black. The oxygen ions are shown by small black dots with atom labels omitting "O" (e.g., "9" for "O9"). The split atom sites for O9 and O4 owing to the Mn2–O bond-length fluctuation are shown by the two small black dots closely located to one another.

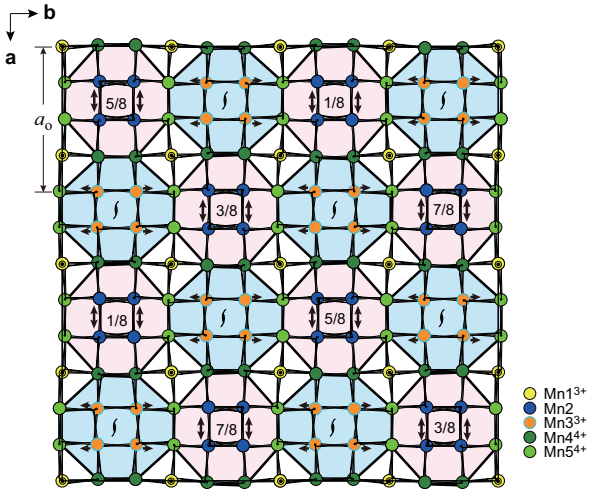

FIGURE 6. The geometrical arrangement of Mn atoms in the orthorhombic $3 \times 3 \times 1$ *Fddd* supercell of the $LiMn_2O_4$ spinel viewed along **c**. The JT-inactive $Mn4^{4+}$ and $Mn5^{4+}$ lie at the vertices of a slightly distorted network of a truncated square tessellation, composed of square and octagonal prisms. The square prism (white) houses Mn1 with JT distortion along **c** (perpendicular to the paper), the octagonal prism (pink) houses the $Mn2_4O9_4$ heterocubane with the JT-induced bond-length fluctuation along **a**, and the other octagonal prism (blue) houses Mn3 with the JT distortion along **b**. The directions of JT distortions are given by small arrows. The *a*-length of the prototype spinel is shown as a_0. The *z*-heights of the $Mn2_4O9_4$ heterocubane center are given as 1/8, 3/8, etc.

polarons are confined in one type of the octagonal prism in the truncated square tessellation of Mn^{4+} ions with spin states opposite to that of Mn2. Note that the $Mn3^{3+}$ ions in the other octagonal prism do not form the heterocubane cluster by themselves, but are aligned like a spiral staircase about the twofold screw axis in the prism (Fig. 6). Since the high-temperature form of $LiMn_2O_4$ has an cubic unit cell of the spinel-type, manganese atoms are expected to have spin and orbital freedoms. The spin blockade achieved by the formation of the truncated square tessellation is broken in the high-temperature form, allowing a free migration of polarons. The cubic–orthorhombic phase transition of $LiMn_2O_4$ near room temperature can thus be regarded as an order–disorder transition of the molecular polarons centered at the Mn_4O_4 heterocubanes. This picture appears to have close relationships with the polaron melting and ordering in the first-order phase transition of the perovskite-type manganite, $Pr_{1-x}Ca_xMnO_3$ ($0.32 \le x \le 0.5$), reported by Jooss et al. (2007).

High-temperature form

The present study revealed a positional disordering of the oxygen ions in the high-temperature form. The disorder can be modeled into the harmonically vibrating split-atom model (the 96*g* model) or the anharmonically vibrating 32*e* model, as mentioned in the Results section. These two models have benefits and drawbacks, although the 96*g* model is practically useful for studies using the powder diffraction technique, in which the anharmonic refinement is often inapproachable.

A drawback of the 96*g* model is the attenuated length of the longer Mn–O bond, as shown in Figure 3. From the EXAFS study assuming the three-shell model, Yamaguchi et al. (1998) reported that the Mn–O bond lengths were 2.23 and 1.92 Å at 300 K in the high-form of $LiMn_2O_4$ and the ratio of the lengths remained almost constant over the high- and low-forms in the temperature range 200–370 K. These Mn–O bond lengths agree well with those in the low form at 230 K in the present study. However, the longer Mn–O bond length [2.070(3) Å at 320 K] of the 96*g* model for the high-form is attenuated from the fully elongated Mn^{3+}–O bond (~2.2 Å) in the low form (Fig. 3), as well as the longer Mn–O bond length (2.23 Å at 300 K) in the high form reported by Yamaguchi et al. (1998). This attenuation appears to arise from the symmetry constraint of the 96*g* model of $Fd\bar{3}m$, which imposes the 4:8 ratio upon the number of longer and shorter Mn–O bonds per two Mn octahedra in $LiMn_2O_4$, though the ratio should be approximately 2:10, as Yamaguchi et al. (1998) assumed in their EXAFS study using the three-shell model.

On the other hand, the anharmonic 32*e* model is advantageous in describing a dynamical variation of the Mn–O bond length, as shown in Figure 7, although the variation can only be visualized by the probability density function of oxygen atoms calculated from the inverse Fourier transform of their anharmonic ADPs.

A common feature about the oxygen ion disorder in the high- and low forms (Fig. 7) is that the oxygen ions are distributed with three main extrusions grasping the circumsphere of the LiO_4 tetrahedron along the directions to stay further from adjacent manganese ions. This similarity about the oxygen ion disordering across the two forms is consistent with the transition mechanism of $LiMn_2O_4$, as stated in the previous section.

The nearly stoichiometric composition of the present crystal agrees with the studies by Rousse et al. (1999a, 1999b), in which δ was determined to be 0.028(26) by the redox titration. The oxygen deficiency of almost null obtained from the harmonic 96*g* and anharmonic 32*e* models is consistent with the stoichiometric composition. In contrast to this, the oxygen deficiency (δ) tends to be evaluated excessively in the harmonic 32*e* model, as mentioned in the Results section. Oxygen ions are statically and/or dynamically displaced from the ideal 32*e* site in an irregular shape, as shown Figure 7. Therefore, it is possible that the population analysis based on the conventional harmonic 32*e* model

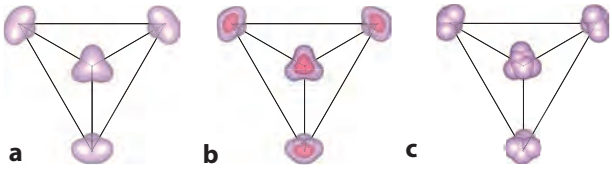

FIGURE 7. Disorder of oxygen ions tetrahedrally surrounding the Li ion in the low- and high-temperature forms of $LiMn_2O_4$ viewed along [111] of the cubic prototype: (**a**) the atomic displacement parameter (ADP) ellipsoids of 12 oxygen ions with 33.3% occupation around Li, obtained from the harmonic 96*g* model for the high-temperature form at 320 K; (**b**) the joint-probability density function (j-pdf) of 4 oxygen ions obtained from the anharmonic (up to the fourth-order) 32*e* model for the high-temperature form at 320 K, and (**c**) the statistical distribution of oxygen ions at 230 K in the low-temperature form, superimposed onto a LiO_4 tetrahedron by translation operation. The ADP ellipsoids in **a** are drawn at the 95% probability level, and the j-pdf of the oxygen ions in **b** is drawn using two isosurfaces of 50 and 95% probability levels from inside, and the oxygen ions in **c** are depicted using spheres of 0.6 Å in radius.

fail to count all the oxygen ions. In this respect, it is necessary to reexamine the relationship between the transition temperatures and oxygen vacancies (δ) reported by Kanno et al. (2001), Tachibana et al. (2003), and Yonemura et al. (2004), because the δ values in these studies were determied by the Rietveld refinement based on the harmonic 32*e* model.

IMPLICATIONS

The high-temperature form of $LiMn_2O_4$ is a central component of the cubically stabilized series of $Li_x(Mn,M)_2O_{4-\delta}$ (M = Mg, Co, etc., $0 \le x \le 2$), which is known as a Li-ion conductor (Park et al. 2010). The Li ion migration is widely believed to occur along the zigzagging pathway connecting the Wyckoff 8*a* and 16*c* sites of $Fd\bar{3}m$; the former is the tetrahedral A site and the latter is the vacant octahedral site in the normal AB_2O_4 spinel (Tateishi et al. 2004a). Therefore, the static and dynamic distortions of the triangular oxygen ion bottleneck at the interface of the AO_4 tetrahedron and the adjacent O_6 octahedron are of great importance in Li ion migration. The bond-length fluctuation of the Mn_4O_4 heterocubane and its migration as a polaron in the high-temperature phase of $LiMn_2O_4$ would be advantageous in opening the bottleneck of the O triangle, because the fluctuation directly affects the positions of oxygen ions forming the bottleneck, as shown in Figure 2b. In practical applications, however, attention should be paid to the distribution in time and space of the oxidation states of Mn, because it may vary depending on *x* and δ, and probably tends to cluster easily, which seriously affects the performance of the Li conduction. As an example, the present study shows that the poor transport property in the $3 \times 3 \times 1$ superstructure of $LiMn_2O_4$, as inferred by Tateishi et al. (2004a), can be ascribed to the formation of the truncated square tessellation of Mn^{4+}, which immobilizes polarons via the spin blockade.

ACKNOWLEDGMENTS

The authors thank Vaclav Petricek at the Institute of Physics, Academy of Science, Czech Republic, for the implementation of the Jana2006 program package. We also appreciate Douglas du Boulay at the University of Western Australia, for the implementation of the Xtal program package, and his help during his stay at our laboratory through the Japan Society for the Promotion of Science (JSPS) fellowship P02148. The synchrotron experiments were carried at the Photon Factory, High Energy Acceleration Research Organization, Tsukuba, based on the programs 2002G042, 2006G242, 2009G005, and 2011G022. This work was supported by JSPS KAKENHI Grant numbers 18206071 (2006–2008) and 22360272 (2010–2013).

REFERENCES CITED

Becker, P.J., and Coppens, P. (1974) Extinction within the limit of validity of the Darwin transfer equations. I. General formalism for primary and secondary extinction and their applications to spherical crystals. Acta Crystallographica Section A, 30, 129–147.

Brandenburg, K., and Putz, H. (2005) DIAMOND Version 3. Crystal Impact GbR, Postfach 1251, D-53002 Bonn, Germany.

Brown, I.D. (2002) The Chemical Bond in Inorganic Chemistry: The Bond Valence Model. Oxford University Press, U.K.

Brown, I.D., and Altermatt, D. (1985) Bond-valence parameters obtained from a systematic analysis of the Inorganic Crystal Structure Database. Acta Crystallographica Section B, 41, 244–247.

Goodenough, J.B., Zhou, J.S., Rivadulla, F., and Winkler, E. (2003) Bond-length fluctuations in transition-metal oxoperovskites. Journal of Solid State Chemistry, 175, 116–123.

Grunbaum, B., and Shephard, G.C. (1987) Tilings and Patterns. Freeman, New York.

Hall, S.R., du Boulay, D.J., and Olthof-Hazekamp, R. (2002) Gnu Xtal System. University of Western Australia, http://xtal.sourceforge.net. Accessed on April 2005.

Jooss, Ch., Wu, L., Beetz, T., Klie, R.F., Beleggia, M., Schofield, M.A., Schramm, S., Hoffmann, J., and Zhu, Y. (2007) Polaron melting and ordering as key mechanisms for colossal resistance effects in manganites. Proceedings of the National Academy of Sciences, 104, 13597–13602.

Kanno, R., Yonemura, M., Kohigashi, T., Kawamoto, Y., Tabuchi, M., and Kamiyama, T. (2001) Synthesis and structures of lithium manganese oxide spinel, $LiMn_2O_{4-\delta}$ ($0 \le \delta \le 0.27$). Journal of Power Sources, 97-98, 423–426.

Kishimoto, S., Ishizawa, N., and Vaalsta, T.P. (1998) A fast detector using stacked avalanche photodiodes for X-ray diffraction experiments with synchrotron radiation. Review of Scientific Instruments, 69, 384–391.

Maignan, A., Caignaert, V., Raveau, B., Khomskii, D., and Sawatzky, G. (2004) Thermoelectric power of $HoBaCo_2O_{5.5}$: Possible evidence of the spin blockade in cobaltites. Physical Review Letters, 93, 026401.

Momma, K., and Izumi, F. (2011) VESTA 3 for three-dimensional visualization of crystal, volumetric and morphology data. Journal of Applied Crystallography, 44, 1272–1276.

Moore, E.A., and Janes, R. (2004) Metal-Ligand Bonding. Royal Society of Chemistry, Cambridge, U.K.

Park, M., Zhang, X., Chung, M., Less, G.B., and Sastry, A.M. (2010) A review of conduction phenomena in Li-ion batteries. Journal of Power Sources, 195, 7904–7929.

Petricek, V., Dusek, M., and Palatinus, L. (2006) Jana2006, The crystallographic computing system. Institute of Physics, Praha, Czech Republic.

Rodríguez-Carvajal, J., Rousse, G., Masquelier, C., and Hervieu, M. (1998) Electronic crystallization in a lithium battery material: Columnar ordering of electrons and holes in the spinel $LiMn_2O_4$. Physical Review Letters, 81, 4660–4663.

Rousse, G., Masquelier, C., Rodríguez-Carvajal, J., and Hervieu, M. (1999a) Cubic–orthorhombic transition in the stoichiometric spinel $LiMn_2O_4$. Electrochemical and Solid-State Letters, 2, 6–8.

Rousse, G., Masquelier, C., Rodríguez-Carvajal, J., Elkaim, E., Lauriat, J.P., and Martínez, J.L. (1999b) X-ray study of the spinel $LiMn_2O_4$ at low temperatures. Chemistry of Materials, 11, 3629–3635.

Sasaki, S. (1989) Anomalous Scattering Factors for Synchrotron Radiation Users, Calculated Using Cromer and Liberman's Method. KEK Report, 88-14, 1–136.

——— (1990) X-Ray Absorption Coefficients of the Elements (Li to Bi, U). KEK Report 90-16, 1–143.

——— (1997) Radial distribution of electron density in magnetite, Fe_3O_4. Acta Crystallographica Section B, 53, 762–766.

Satow, Y., and Iitaka, Y. (1989) Horizontal-type four-circle diffractometer station of the vertical wiggler beamline at the Photon Factory. Review of Scientific Instruments, 60, 2390–2393.

Senn, M.S., Wright, J.P., and Attfield, J.P. (2012) Charge order and three-site distortions in the Verwey structure of magnetite. Nature, 481, 173–176.

Tachibana, M., Tojo, T., Kawaji, H., Atake, T., Yonemura, M., and Kanno, R. (2003) Heat capacity of $LiMn_2O_{4-\delta}$: Effect of oxygen content on charge and magnetic ordering. Physical Review B, 68, 094421.

Takahashi, Y., Akimoto, J., Gotoh, Y., Dokko, K., Nishizawa, M., and Uchida, I. (2003) Structure and electron density analysis of lithium manganese oxides by single-crystal X-ray diffraction. Journal of the Physical Society of Japan, 72, 1483–1490.

Tateishi, K., du Boulay, D., and Ishizawa, N. (2004a) The effect of mixed Mn valences on Li migration in $LiMn_2O_4$ spinel: A molecular dynamics study. Applied Physics Letters, 84, 529–531.

Tateishi, K., Suda, K., du Boulay, D., Ishizawa, N., and Oishi, S. (2004b) $LiMn_2O_4$: a spinel-related low-temperature modification. Acta Crystallographica Section E, 60, i18–i21.

Vaalsta, T.P., and Hester, J.R. (1997) Diff14A Software. Photon Factory, KEK, Tsukuba, Japan.

Verwey, E.J.W., and de Boer, J.H. (1936) Cation arrangement in a few oxides with crystal structures of the spinel type. Recueil des Travaux Chimiques des Pays-Bas, 55, 531–540.

Verwey, E.J.W., and Haayman, P.W. (1941) Electronic conductivity and transition point of magnetite ("Fe_3O_4"). Physica, 8, 979–987.

Weinmann, D., Häusler, W., and Kramer, B. (1995) Spin blockades in linear and nonlinear transport through quantum dots. Physical Review Letters, 74, 984–987.

Yamada, A., and Tanaka, M. (1995) Jahn-Teller structural phase transition around 280 K in $LiMn_2O_4$. Materials Research Bulletin, 30, 715–721.

Yamada, Y., Mori, M., Noda, Y., and Iizumi, M. (1979) Neutron diffuse scattering in Fe_3O_4 due to molecular polarons. Solid State Communications, 32, 827–830.

Yamaguchi, H., Yamada, A., and Uwe, H. (1998) Jahn-Teller transition of $LiMn_2O_4$ studied by X-ray-absorption spectroscopy. Physical Review B, 58, 8–11.

Yonemura, M., Yamada, A., Kobayashi, H., Tabuchi, M., Kamiyama, T., Kawamoto, Y., and Kanno, R. (2004) Synthesis, structure, and phase relationship in lithium manganese oxide spinel. Journal of Materials Chemistry, 14, 1948–1958.

MANUSCRIPT SUBMITTED DECEMBER 11, 2013
MANUSCRIPT ACCEPTED MARCH 20, 2014
MANUSCRIPT HANDLED BY HIROSHI KOJITANI